A new three-dimensional higher-order thermomechanical ice sheet model: Basic sensitivity, ice stream development, and ice flow across subglacial lakes

Frank Pattyn

Department of Geography, Vrije Universiteit Brussel, Brussels, Belgium

Received 29 November 2002; revised 27 March 2003; accepted 17 April 2003; published 16 August 2003.

[1] A new three-dimensional thermomechanically coupled ice sheet model is developed. Contrary to the majority of three-dimensional ice sheet models (shallow ice approximation), higher-order stress gradients (longitudinal and transverse) are accounted for in the force balance equations. The horizontal velocity field is determined from the force balance equations in their "derivative form" (elliptical equation) using the method presented by *Pattyn* [2000, 2002a]. The model is solved on a regular grid in the horizontal and an irregular grid in the vertical and is numerically stable. Basic experiments include the European Ice Sheet Modeling Initiative (EISMINT) benchmarks for large-scale ice sheet models and a comparison with the Saito-Blatter ice sheet model including higher-order stress gradients [*Saito et al.*, 2003]. Detailed calculations of ice flow over three-dimensional bedrock perturbations showed the validity of the higher-order solution. The model is capable of simulating the evolution of an ice stream within the ice sheet and shows important aspects of observed ice stream features, such as the surface flattening and the importance of side drag. The simulation of the ice flow over a subglacial lake results in a flattening of the surface, a local velocity increase over the lake, and a deviation of the ice flow from the main flow direction, features which are also observed at Lake Vostok, Antarctica. *INDEX TERMS:* 1827 Hydrology: Glaciology (1863); 1863 Hydrology: Snow and ice (1827); 3230 Mathematical Geophysics: Numerical solutions; *KEYWORDS:* higher-order, ice sheet model, thermomechanical, ice stream, subglacial lake

Citation: Pattyn, F., A new three-dimensional higher-order thermomechanical ice sheet model: Basic sensitivity, ice stream development, and ice flow across subglacial lakes, *J. Geophys. Res.*, *108*(B8), 2382, doi:10.1029/2002JB002329, 2003.

1. Introduction

[2] Most ice sheet models are based on the so-called "shallow ice approximation" (SIA) [*Hutter*, 1983], which is valid for an ice mass with a small aspect ratio ($H \ll L$), where flow is dominated by internal shear deformation: ice flow is driven by gravity, and vertical shearing is concentrated close to the bedrock. Almost no shearing exists close to the surface. However, the SIA is not valid at all places in an ice sheet, such as at the ice divide or near the ice sheet margin [*Baral et al.*, 2001]. Below the ice divide there is theoretically no shearing present. This would mean that according to the SIA and for a Glen-type rheology, the effective stress becomes zero, implying an infinitely large viscosity so that the free surface is stiff against shearing. This is not realistic as longitudinal stresses must develop which enhance the effective stress and lower the viscosity. This effect goes beyond the lowest order of the shallow ice approximation [*Baral et al.*, 2001]. A precise knowledge on the stress field underneath an ice divide is of importance to derive the vertical velocity, which determines age versus depth, thinning of the stratigraphic layers by vertical strain, and vertical advection of heat [*Dansgaard and Johnsen*, 1969]. Numerical calculations have shown that the profiles of velocity versus depth have different shapes at divides compared to flank positions [*Raymond*, 1983; *Schøtt Hvidberg*, 1996].

[3] Near the margin of ice sheets (which comprises grounding lines, transition zones, outlet glaciers and ice streams), all forces in the force balance become equally important, especially when basal sliding comes into play or even dominates the horizontal flow field. Longitudinal stretching and lateral shearing play an essential role in the dynamics of large outlet glaciers and major Antarctic ice streams. The governing processes near the margin involve a reduction of the basal drag, leading to significant basal motion (due to sliding and/or basal sediment deformation), which increases the complexity of the problem. Furthermore, thermomechanical control amplifies this complexity which might even lead to channeling of ice flow [*Hindmarsh*, 2001].

[4] However, all these feedback processes are not clearly understood as thermomechanical models that solve the

0148-0227/03/2002JB002329$09.00

Stokes problem in three dimensions are not widely developed. Present-day three-dimensional numerical ice sheet models including full thermomechanical coupling are those developed by *Huybrechts* [1990], *Ritz et al.* [1997], *Greve* [1997], or *Marshall and Clarke* [1997], to name a few. All these models have been successfully applied to simulate major present and paleo-ice sheet behavior on the globe. They are all based on the SIA and do not include longitudinal nor transverse stress gradients in a systematic way. The transition zone between different flow types (e.g., between ice sheet and ice shelf flow, or the onset regions of ice streams) is often not properly accounted for, even though all stresses and stress gradients are of equal importance in the force balance. Three-dimensional thermomechanically coupled ice sheet models including higher-order stress gradients are sparsely seeded. Among them are the models of *Mayer* [1996], *Albrecht* [2000] and *Saito* [2002], the latter two based on the model by *Blatter* [1995] and *Colinge and Blatter* [1998]. The reason for this sparsity must be sought in the complexity of the model description, the difficulty to obtain a numerically stable result, and the high computational cost, despite the exponential increase over time of computer power.

[5] This paper presents the mathematical and numerical details of a new three-dimensional higher-order model (HO model; including longitudinal and transverse stress gradients) with full thermomechanical coupling. It is based on a two-dimensional version developed earlier [*Pattyn*, 2000, 2002a]. Although transverse stresses and their gradients are properly accounted for, some assumptions are made, such as neglecting the variational stress term. An approach different from that of *Blatter* [1995] was taken to obtain a solution to the force balance equations. Basic experiments with the model include the standard European Ice Sheet Modeling Initiative (EISMINT) I benchmark experiments [*Huybrechts et al.*, 1996] as well the EISMINT II experiments with thermomechanical coupling [*Payne et al.*, 2000]. Special attention is paid to the flow field underneath the ice divide and a comparison is made with a similar 3-D model according to the SIA. Both experiments with and without (isotherm) thermomechanical coupling are considered. Furthermore, the flow over small-scale bedrock perturbations is considered in a diagnostic model experiment. The evolution of an ice stream is investigated as well as the ice flow over a subglacial lake, such as Lake Vostok, Antarctica.

2. Field Equations

[6] The model approach is based on continuum thermodynamic modeling, and encompasses balance laws of mass, momentum and energy, extended with a constitutive equation. Treating ice as an incompressible fluid with constant density, the equations for conservation of mass, momentum and energy are written as

$$\nabla \cdot \mathbf{v} = 0, \tag{1}$$

$$\rho \frac{\mathrm{d}\mathbf{v}}{\mathrm{d}t} = \nabla \cdot \sigma + \rho \mathbf{g}, \tag{2}$$

$$\rho \frac{\mathrm{d}(c_p \theta)}{\mathrm{d}t} = \nabla (k_i \nabla \theta) + \Phi, \tag{3}$$

Table 1. Constants Used in the Numerical Model

Symbol	Constant	Value	Units
β	dependence of melting on pressure	9.8×10^{-8}	K Pa^{-1}
ρ	ice density	910	kg m^{-3}
B_0	flow rate factor	2.207	Pa a$^{1/n}$
C	flow rate factor	0.16612	K^K
G	geothermal heat flux	4.2×10^{-2}	W m^{-2}
K	flow rate exponent	1.17	
L	specific latent heat of fusion	3.35×10^5	J kg^{-1}
Q	activation energy for creep	7.88×10^4	J mol^{-1}
R	universal gas constant	8.31	J mol^{-1} K^{-1}
θ_r	limit temperature in flow rate factor	273.39	K
c_p	heat capacity of ice	2009	J kg^{-1} K^{-1}
g	gravitational constant	9.81	m s^{-2}
k_i	thermal conductivity of ice	6.62×10^{-7}	J m^{-1} K^{-1} yr^{-1}
m	enhancement factor in flow law	1	
n	exponent in Glen's flow law	3	

where ρ is the ice density, $\mathbf{g}$ is gravitational acceleration, $\mathbf{v}$ is the velocity vector, $[\sigma]$ is the stress tensor, θ is the ice temperature, c_p and k_i are the heat capacity and thermal conductivity of the ice, respectively, and Φ is internal frictional heating due to deformation. Values for constants used in this paper are given in Table 1. Considering a Cartesian coordinate system (x, y, z) with the z axis vertically pointing upward ($z = 0$ at sea level), and denoting the velocity components in either direction as u, v, and w, the conservation of mass equation (1) can be rewritten as

$$\frac{\partial u}{\partial x} + \frac{\partial v}{\partial y} + \frac{\partial w}{\partial z} = 0. \tag{4}$$

Neglecting acceleration terms in equation (2) and considering the gravitational acceleration only important in the vertical direction, the linear momentum becomes

$$\frac{\partial \sigma_{xx}}{\partial x} + \frac{\partial \sigma_{xy}}{\partial y} + \frac{\partial \sigma_{xz}}{\partial z} = 0, \tag{5}$$

$$\frac{\partial \sigma_{yx}}{\partial x} + \frac{\partial \sigma_{yy}}{\partial y} + \frac{\partial \sigma_{yz}}{\partial z} = 0, \tag{6}$$

$$\frac{\partial \sigma_{zx}}{\partial x} + \frac{\partial \sigma_{zy}}{\partial y} + \frac{\partial \sigma_{zz}}{\partial z} = \rho g. \tag{7}$$

As a complete solution to the stress equilibrium equations (5)–(7) is quite complicated, these equations are solved in a somewhat reduced form. The major assumption to the force balance equations is to apply the hydrostatic approximation in the vertical, so that equation (7) reduces to

$$\frac{\partial \sigma_{zz}}{\partial z} \cong \rho g. \tag{8}$$

This implies that the variational stress is neglected, i.e., the resistance to a varying stress gradient in the direction of motion (the so-called T term) in the vertically integrated force budget [*Budd*, 1970a, 1970b, 1971]. This term is also

known as the vertical resistive stress [*Van der Veen and Whillans*, 1989]. Numerical calculations have shown that vertical resistive stress occurs in regions where the flow regime changes, such as near the ice divide or near the margin, but that this stress component is almost 2 orders of magnitude smaller than other normal and shear stress components [*Pattyn*, 2000]. Normal stress deviators are not neglected and accounted for properly. Neglecting atmospheric pressure, an expression for σ_{zz} is obtained by integrating equation (8) from the surface s to a height z in the ice body. Since the flow relation (see below) is unaffected by hydrostatic pressure it is convenient to work with stress deviators. The stress deviator components are obtained by subtracting the amplitude of the hydrostatic pressure, $\sigma'_{ij} = \sigma_{ij} - \frac{1}{3}\delta_{ij}\sum_k \sigma_{kk}$, where δ_{ij} is the Kronecker delta. Inserting the stress deviator components and assuming a zero normal stress at the surface, the horizontal force balance equations (5) and (6) become after some algebraic manipulation

$$\frac{\partial}{\partial x}\left(2\sigma'_{xx} + \sigma'_{yy}\right) + \frac{\partial \sigma'_{xy}}{\partial y} + \frac{\partial \sigma'_{xz}}{\partial z} = \rho g \frac{\partial s}{\partial x}, \tag{9}$$

$$\frac{\partial}{\partial y}\left(2\sigma'_{yy} + \sigma'_{xx}\right) + \frac{\partial \sigma'_{xy}}{\partial x} + \frac{\partial \sigma'_{yz}}{\partial z} = \rho g \frac{\partial s}{\partial y}. \tag{10}$$

The constitutive equation governing the creep of polycrystalline ice and relating the deviatoric stresses to the strain rates is taken as a Glen-type flow law with exponent $n = 3$ [*Paterson*, 1994]

$$\sigma'_{ij} = 2\eta\dot{\varepsilon}_{ij}, \quad \eta = \frac{1}{2}A(\theta^*)^{-1/n}\left(\dot{\varepsilon} + \dot{\varepsilon}_0\right)^{(1-n)/n}, \tag{11}$$

where $\dot{\varepsilon}$ is the second invariant of the strain rate tensor, defined by $\dot{\varepsilon}^2 = \sum_{ij}\frac{1}{2}\dot{\varepsilon}_{ij}\dot{\varepsilon}_{ij}$ and η is the effective viscosity. $\dot{\varepsilon}_0$ is a small number (10^{-30}) to make the viscosity finite. When using a power law rheology, as is the case with Glen's flow law, a singularity might occur at the bed under a divide (no shearing) when no slip boundary conditions hold. The use of such a small number does not influence the numerical outcome of the model. The flow law rate factor $A(\theta^*)$ is a function of temperature, where θ^* is the ice temperature (K) corrected for pressure melting, i.e., $\theta^* = \theta + \beta P$, and where P is the ice pressure ($P = \sigma'_{xx} + \sigma'_{yy} - \rho g\,(s - z)$). Following *Hooke* [1981], $A(\theta^*)$ is parameterized as an Arrhenius relationship:

$$A(\theta^*) = m\left(\frac{1}{B_0}\right)^n \exp\left(\frac{3C}{(\theta_r - \theta^*)^K} - \frac{Q}{R\theta^*}\right). \tag{12}$$

Here Q is the activation energy for ice creep, R is the universal gas constant, and m is an enhancement factor (or tuning parameter). By definition, strain rates are related to velocity gradients, so that

$$\begin{pmatrix} \dot{\varepsilon}_{xx} & \dot{\varepsilon}_{xy} & \dot{\varepsilon}_{xz} \\ \dot{\varepsilon}_{yx} & \dot{\varepsilon}_{yy} & \dot{\varepsilon}_{yz} \\ \dot{\varepsilon}_{zx} & \dot{\varepsilon}_{zy} & \dot{\varepsilon}_{zz} \end{pmatrix} = \begin{pmatrix} \frac{\partial u}{\partial x} & \frac{1}{2}\left(\frac{\partial u}{\partial y} + \frac{\partial v}{\partial x}\right) & \frac{1}{2}\frac{\partial u}{\partial z} \\ \frac{1}{2}\left(\frac{\partial u}{\partial y} + \frac{\partial v}{\partial x}\right) & \frac{\partial v}{\partial y} & \frac{1}{2}\frac{\partial v}{\partial z} \\ \frac{1}{2}\frac{\partial u}{\partial z} & \frac{1}{2}\frac{\partial v}{\partial z} & \frac{\partial w}{\partial z} \end{pmatrix}. \tag{13}$$

Here, another assumption is made, i.e., that horizontal gradients of the vertical velocity are small compared to the vertical gradient of the horizontal velocity, or $\partial w/\partial x \ll \partial u/\partial z$ and $\partial w/\partial y \ll \partial v/\partial z$. This is a common assumption in ice sheet modeling, and is valid for most of the ice sheet domain. Making use of the principle of mass conservation equation (4), the effective strain rate is written as

$$\dot{\varepsilon} = \left(\dot{\varepsilon}^2_{xx} + \dot{\varepsilon}^2_{yy} + \dot{\varepsilon}_{xx}\dot{\varepsilon}_{yy} + \dot{\varepsilon}^2_{xy} + \dot{\varepsilon}^2_{xz} + \dot{\varepsilon}^2_{yz}\right)^{\frac{1}{2}}. \tag{14}$$

Combining the flow law equation (11) and the horizontal stress field equations (9) and (10), and replacing the strain rate components by velocity gradients using equations (13) and (14), one obtains

$$\frac{\partial}{\partial x}\left(4\eta\frac{\partial u}{\partial x} + 2\eta\frac{\partial v}{\partial y}\right) + \frac{\partial}{\partial y}\left(\eta\frac{\partial u}{\partial y} + \eta\frac{\partial v}{\partial x}\right) + \frac{\partial}{\partial z}\left(\eta\frac{\partial u}{\partial z}\right) = \rho g\frac{\partial s}{\partial x}, \tag{15}$$

$$\frac{\partial}{\partial y}\left(4\eta\frac{\partial v}{\partial y} + 2\eta\frac{\partial u}{\partial x}\right) + \frac{\partial}{\partial x}\left(\eta\frac{\partial u}{\partial y} + \eta\frac{\partial v}{\partial x}\right) + \frac{\partial}{\partial z}\left(\eta\frac{\partial v}{\partial z}\right) = \rho g\frac{\partial s}{\partial y}, \tag{16}$$

where

$$\eta = \frac{1}{2}A(\theta^*)^{-1/n}\left\{\left(\frac{\partial u}{\partial x}\right)^2 + \left(\frac{\partial v}{\partial y}\right)^2 + \frac{\partial u}{\partial x}\frac{\partial v}{\partial y} + \frac{1}{4}\left(\frac{\partial u}{\partial y} + \frac{\partial v}{\partial x}\right)^2 + \frac{1}{4}\left(\frac{\partial u}{\partial z}\right)^2 + \frac{1}{4}\left(\frac{\partial v}{\partial z}\right)^2 + \dot{\varepsilon}_0^2\right\}^{(1-n)/2n}. \tag{17}$$

Expanding equations (15) and (16) and rearranging terms, leads to

$$4\frac{\partial \eta}{\partial x}\frac{\partial u}{\partial x} + \frac{\partial \eta}{\partial y}\frac{\partial u}{\partial y} + \frac{\partial \eta}{\partial z}\frac{\partial u}{\partial z} + \eta\left(4\frac{\partial^2 u}{\partial x^2} + \frac{\partial^2 u}{\partial y^2} + \frac{\partial^2 u}{\partial z^2}\right) = \rho g\frac{\partial s}{\partial x} - 2\frac{\partial \eta}{\partial x}\frac{\partial v}{\partial y} - \frac{\partial \eta}{\partial y}\frac{\partial v}{\partial x} - 3\eta\frac{\partial^2 v}{\partial x \partial y}, \tag{18}$$

$$4\frac{\partial \eta}{\partial y}\frac{\partial v}{\partial y} + \frac{\partial \eta}{\partial x}\frac{\partial v}{\partial x} + \frac{\partial \eta}{\partial z}\frac{\partial v}{\partial z} + \eta\left(4\frac{\partial^2 v}{\partial y^2} + \frac{\partial^2 v}{\partial x^2} + \frac{\partial^2 v}{\partial z^2}\right) = \rho g\frac{\partial s}{\partial y} - 2\frac{\partial \eta}{\partial y}\frac{\partial u}{\partial x} - \frac{\partial \eta}{\partial x}\frac{\partial u}{\partial y} - 3\eta\frac{\partial^2 u}{\partial x \partial y}, \tag{19}$$

An expression for the vertical velocity w is obtained through vertical integration of the incompressibility condition (4) from the base of the glacier to a height z

$$w(z) - w(b) = -\int_b^z \left(\frac{\partial u}{\partial x} + \frac{\partial v}{\partial y}\right)\mathrm{d}z. \tag{20}$$

Neglecting horizontal diffusion, the energy balance equation (3) is written as

$$\rho c_p\frac{\partial \theta}{\partial t} = k_i\frac{\partial^2 \theta}{\partial z^2} - \rho c_p\left(u\frac{\partial \theta}{\partial x} + v\frac{\partial \theta}{\partial y} + w\frac{\partial \theta}{\partial z}\right) + 2\dot{\varepsilon}\sigma, \tag{21}$$

where σ is the effective stress or the second invariant of the stress tensor. The heat transfer is thus a result of vertical diffusion, horizontal and vertical advection, and internal deformational heating.

[7] Using a kinematic boundary condition at the upper and lower surface of the ice mass (see below), the mass balance equation (1) is integrated along the vertical in order to obtain an expression for the change of local ice thickness in space

$$\frac{\partial H}{\partial t} = -\nabla \int_b^s \mathbf{u} \mathrm{d}z + M_s - M_b = -\nabla(\bar{\mathbf{u}} H) + M_s - M_b, \quad (22)$$

where $\mathbf{u}$ is the horizontal velocity vector (m yr^{-1}), H is the ice thickness (m), M_s is the local accumulation-ablation function (m yr^{-1} ice equivalent), and M_b is the melting rate at the base of the glacier (m yr^{-1}). Negative values of M_b imply refreezing, which is not considered here. Local ice thickness variations are thus in balance with the divergence of the ice flux and the net input of mass at the upper and lower surface of the ice mass.

[8] In order to verify the results of the HO model, a "shallow ice" model was implemented as well. According to the SIA the horizontal velocity field is defined as [e.g., *Huybrechts et al.*, 1996; *Payne et al.*, 2000]

$$\mathbf{u}(z) = -2(\rho g)^n |\nabla s|^{n-1} \nabla s \int_b^z A(\theta^*)(s-z)^n \mathrm{d}z + \mathbf{u}_b. \quad (23)$$

Note that according to the SIA the velocity is obtained through vertical integration over the ice column and is only a function of the local geometry of the ice mass.

3. Boundary Conditions

[9] Boundary conditions to the ice mass are zero ice thickness ($H = 0$) at the edges of the model domain, a stress-free surface and no-slip boundary condition at the base ($u_b = v_b = 0$). In some of the experiments below a stress-free boundary condition was applied at some grid points of the numerical domain (free-slip condition or zero traction). These two treatments of basal conditions represent only the most extreme end-members of reality and are not applicable to many natural situations (including ice streams, where basal drag is small but not zero). However, such conditions make it easier to compare the model with benchmark tests. Using extreme boundary conditions pushes the model to its limits of application and demonstrate its performance in terms of numerical stability under such extreme conditions. Experiments carried out with varying basal traction (according to a sliding law) resulted in more realistic simulations, but did not alter the general performance of the model as shown in the experiments below.

[10] The kinematic boundary conditions at the lower ice surface reads

$$w(b) = \frac{\partial b}{\partial t} + \mathbf{u}_b \nabla b - M_b. \quad (24)$$

Starting from the vertical velocity at the base (according to equation (24)), equation (20) is numerically integrated to the surface. The basal drag is defined as the sum of all basal resistive forces and written as [*Van der Veen and Whillans*, 1989]

$$\tau_{bx} = \sigma'_{xz}(b) - \left(2\sigma'_{xx}(b) + \sigma'_{yy}(b)\right)\frac{\partial b}{\partial x} - \sigma'_{xy}(b)\frac{\partial b}{\partial y}, \quad (25)$$

$$\tau_{by} = \sigma'_{yz}(b) - \left(2\sigma'_{yy}(b) + \sigma'_{xx}(b)\right)\frac{\partial b}{\partial y} - \sigma'_{xy}(b)\frac{\partial b}{\partial x}. \quad (26)$$

The stress-free surface implies that [*Van der Veen and Whillans*, 1989]

$$\left(2\sigma'_{xx}(s) + \sigma'_{yy}(s)\right)\frac{\partial s}{\partial x} + \sigma'_{xy}\frac{\partial s}{\partial y} - \sigma_{xz}(s) = 0 \quad (27)$$

$$\left(2\sigma'_{yy}(s) + \sigma'_{xx}(s)\right)\frac{\partial s}{\partial y} + \sigma'_{xy}\frac{\partial s}{\partial x} - \sigma_{yz}(s) = 0. \quad (28)$$

Written in terms of velocity gradients, this results in

$$\left(4\frac{\partial u}{\partial x} + 2\frac{\partial v}{\partial y}\right)\frac{\partial s}{\partial x} + \left(\frac{\partial u}{\partial y} + \frac{\partial v}{\partial x}\right)\frac{\partial s}{\partial y} - \frac{\partial u}{\partial z} = 0, \quad (29)$$

$$\left(4\frac{\partial v}{\partial y} + 2\frac{\partial u}{\partial x}\right)\frac{\partial s}{\partial y} + \left(\frac{\partial u}{\partial y} + \frac{\partial v}{\partial x}\right)\frac{\partial s}{\partial x} - \frac{\partial v}{\partial z} = 0. \quad (30)$$

A similar expression can be obtained for a stress-free base, as is the case in an ice shelf or an ice stream, simply by replacing s in equations (29) and (30) by b. Boundary conditions to the thermodynamic equation (21) follow from the mean annual air temperature at the surface. At the base, the temperature gradient is defined as

$$\frac{\partial \theta_b}{\partial z} = -\frac{G + \tau_\mathrm{b} \mathbf{u}_\mathrm{b}}{k_i}, \quad (31)$$

where G is the geothermal heat flux. However, a constant geothermal heat flux is not strictly correct; it might be more realistic to consider heat conduction in the bedrock, so that $G = -k_r (\partial T/\partial z)$, where k_r is the thermal conductivity in the underlying bedrock. However, a constant value of G is a common boundary condition in ice sheet and glacier models, and facilitates model intercomparison according to the EISMINT benchmarks. The basal temperature in the ice mass is kept at the pressure melting point whenever it is reached, and the basal melt rate M_b is calculated as

$$M_b = \frac{1}{\rho L}\left(k_i \frac{\partial \theta_b}{\partial z}|_c + G + \mathbf{u}_b \tau_\mathbf{b}\right), \quad (32)$$

where L is the specific latent heat of fusion and the subscript c stands for the temperature gradient after correction for pressure melting.

4. Coordinate Transformation

[11] For numerical convenience a dimensionless vertical coordinate is introduced to account for ice thickness variations, and which is defined as $\zeta \equiv (s - z)/H$, so that

$\zeta = 0$ at the upper surface and $\zeta = 1$ at the base of the ice mass. The coordinate transformation maps $(x, y, z) \rightarrow (x', y', \zeta)$, so that the function derivatives transform to [*Lliboutry*, 1987]

$$\frac{\partial f}{\partial x} \equiv \frac{\partial f}{\partial x'}\frac{\partial x'}{\partial x} + \frac{\partial f}{\partial y'}\frac{\partial y'}{\partial x} + \frac{\partial f}{\partial \zeta}\frac{\partial \zeta}{\partial x}. \tag{33}$$

Similar expressions are obtained for $\partial f/\partial y$ and $\partial f/\partial z$. A further assumption is made that $\partial x'/\partial x$, $\partial y'/\partial y \cong 1$, and $\partial x'/\partial y$, $\partial x'/\partial z$, $\partial y'/\partial x$, $\partial y'/\partial z \cong 0$, which is valid as long as surface and bedrock gradients are not too large. The function derivatives can thus be rewritten as

$$\frac{\partial f}{\partial x} \equiv \frac{\partial f}{\partial x'} + a_x\frac{\partial f}{\partial \zeta}, \tag{34}$$

$$\frac{\partial^2 f}{\partial x^2} \equiv \frac{\partial^2 f}{\partial x'^2} + b_x\frac{\partial f}{\partial \zeta} + a_x^2\frac{\partial^2 f}{\partial \zeta^2} + 2a_x\frac{\partial^2 f}{\partial x'\partial \zeta}, \tag{35}$$

$$\frac{\partial f}{\partial z} \equiv -\frac{1}{H}\frac{\partial f}{\partial \zeta}, \tag{36}$$

$$\frac{\partial^2 f}{\partial z^2} \equiv \frac{1}{H^2}\frac{\partial^2 f}{\partial \zeta^2}, \tag{37}$$

$$\frac{\partial^2 f}{\partial x \partial z} \equiv \frac{1}{H}\left(\frac{1}{H}\frac{\partial H}{\partial x'}\frac{\partial f}{\partial \zeta} - \frac{\partial^2 f}{\partial x'\partial \zeta} - a_x\frac{\partial^2 f}{\partial \zeta^2}\right), \tag{38}$$

$$\frac{\partial^2 f}{\partial x \partial y} \equiv \frac{\partial^2 f}{\partial x'\partial y'} + c_{xy}\frac{\partial f}{\partial \zeta} + a_y\frac{\partial^2 f}{\partial x'\partial \zeta} + a_x\frac{\partial^2 f}{\partial y'\partial \zeta} + a_x a_y\frac{\partial^2 f}{\partial \zeta^2}, \tag{39}$$

where

$$a_x = \frac{1}{H}\left(\frac{\partial s}{\partial x'} - \zeta\frac{\partial H}{\partial x'}\right), \tag{40}$$

$$b_x = \frac{\partial a_x}{\partial x'} + a_x\frac{\partial a_x}{\partial \zeta} = \frac{1}{H}\left(\frac{\partial^2 s}{\partial x'^2} - \zeta\frac{\partial^2 H}{\partial x'^2} - 2a_x\frac{\partial H}{\partial x'}\right), \tag{41}$$

$$c_{xy} = \frac{\partial a_y}{\partial x'} + a_x\frac{\partial a_y}{\partial \zeta} \equiv \frac{\partial a_x}{\partial y'} + a_y\frac{\partial a_x}{\partial \zeta}. \tag{42}$$

Similar expressions can be obtained for $\partial f/\partial y$, $\partial^2 f/\partial y^2$, $\partial^2 f/\partial y\,\partial z$, a_y, and b_y. The incompressibility condition (4) thus becomes

$$\frac{\partial w}{\partial \zeta} = H\left(\frac{\partial u}{\partial x'} + a_x\frac{\partial u}{\partial \zeta} + \frac{\partial v}{\partial y'} + a_y\frac{\partial v}{\partial \zeta}\right). \tag{43}$$

Making use of equations (34) to (42), equation (18) then becomes after coordinate transformation (equation (19) is transformed accordingly):

$$\begin{aligned} &4\eta_{x'}\frac{\partial u}{\partial x'} + \eta_{y'}\frac{\partial u}{\partial y'} + 4\eta\frac{\partial^2 u}{\partial x'^2} \\ &\quad + \left(4a_x\eta_{x'} + \eta(4b_x + b_y) + a_y\eta_{y'} + \frac{1}{H^2}\frac{\partial \eta}{\partial \zeta}\right)\frac{\partial u}{\partial \zeta} \\ &\quad + \eta\frac{\partial^2 u}{\partial y'^2} + \eta\left(4a_x^2 + a_y^2 + \frac{1}{H^2}\right)\frac{\partial^2 u}{\partial \zeta^2} + 8a_x\eta\frac{\partial^2 u}{\partial x'\partial \zeta} \\ &\quad + 2a_y\eta\frac{\partial^2 u}{\partial y'\partial \zeta} = \rho g\frac{\partial s}{\partial x'} - \eta_{y'}\frac{\partial v}{\partial x'} - 2\eta_{x'}\frac{\partial v}{\partial y'} \\ &\quad - \left(2a_y\eta_{x'} + a_x\eta_{y'} + 3c_{xy}\eta\right)\frac{\partial v}{\partial \zeta} - 3a_x a_y\eta\frac{\partial^2 v}{\partial \zeta^2} \\ &\quad - 3\eta\frac{\partial^2 v}{\partial x'\partial y'} - 3a_y\eta\frac{\partial^2 v}{\partial x'\partial \zeta} - 3a_x\eta\frac{\partial^2 v}{\partial y'\partial \zeta}, \end{aligned} \tag{44}$$

where

$$\eta_{x'} = \frac{\partial \eta}{\partial x'} + a_x\frac{\partial \eta}{\partial \zeta}. \tag{45}$$

[12] Similarly, the upper boundary condition (29) becomes

$$\begin{aligned} &4\frac{\partial s}{\partial x'}\frac{\partial u}{\partial x'} + \frac{\partial s}{\partial y'}\frac{\partial u}{\partial y'} + \left(4a_x\frac{\partial s}{\partial x'} + a_y\frac{\partial s}{\partial y'} + \frac{1}{H}\right)\frac{\partial u}{\partial \zeta} \\ &\quad = -\frac{\partial s}{\partial y'}\frac{\partial v}{\partial x'} - 2\frac{\partial s}{\partial x'}\frac{\partial v}{\partial y'} - \left(2a_y\frac{\partial s}{\partial x'} + a_x\frac{\partial s}{\partial y'}\right)\frac{\partial v}{\partial \zeta}. \end{aligned} \tag{46}$$

[13] Similar transformations are carried out for equation (30), as well as for the strain rate definition (13). Finally, the thermodynamic equation (21) is transformed as follows:

$$\begin{aligned} &\frac{\partial \theta}{\partial t} + \frac{\partial \theta}{\partial \zeta}\left[a_x u + a_y v + \frac{1}{H}\left(\frac{\partial s}{\partial t} - \zeta\frac{\partial H}{\partial t} - w\right)\right] \\ &\quad + u\frac{\partial \theta}{\partial x'} + v\frac{\partial \theta}{\partial y'} - \frac{k}{H^2\rho c_p}\frac{\partial^2 \theta}{\partial \zeta^2} = \frac{2}{\rho c_p}\dot{\varepsilon}\sigma. \end{aligned} \tag{47}$$

[14] Equations (46) to (47) are solved on a regular grid in x' and y', and an irregular grid in ζ. First and second central difference approximations on a regular and irregular grid are given by *Pattyn* [2002a]. At the surface boundaries (e.g., $k = 1$ and $k = N_\zeta$), first and second derivatives are computed using three-point upstream differences. With the exception of the surface boundaries, central differences are used everywhere. Using central differences leads to numerically stable solutions as long as the ice flow is relatively slow (e.g. ice sheet flow, ice flow at transition zones or grounding lines). Whenever the ice moves considerably faster, i.e., for model experiments where velocities of >1000 m yr^{-1} are encountered, three-point upstream differences are applied over the whole model domain for determining horizontal

velocity gradients in the nonlinear viscosity term η, to yield a stable solution.

5. Numerical Solution

5.1. Velocity Field

[15] The basic problem is the determination of the velocity field **v** in an ice mass. The problem is reduced to determining the velocity in the horizontal direction $\mathbf{u}(u, v)$, as the vertical velocity is obtained from the incompressibility condition (4), using the kinematic boundary condition at the lower surface (equation (24)). Although the problem is in itself a nonlinear one, equation (44) can be treated as a pair of coupled linear equations with u (and v) as unknowns, if η is approximated from the previous iteration. The nonlinear part is given by the term η in above equations, which is in itself a function of u and v through the effective strain rate in the nonlinear flow law. The problem is thus twofold: (1) solving a linear set of equations using an estimate of the horizontal velocity field and (2) iterating the nonlinear part by updating η with new estimates of u and v.

5.1.1. Solving Sparse Linear Systems

[16] The finite difference notation of the transformed differential equations for u and v (equation (44)) form a set of linear equations with $u(x', y', \zeta)$ and $v(x', y', \zeta)$ as unknowns. There are two ways to proceed. The easiest way is to solve equation (44) for u, based on estimates for η and v. Subsequently, the related equation for the velocity in the transverse direction is solved for v, based on previous estimates for η and u. A more complex way of solving this set of equations is by solving both equations at once for u and v. The coefficient matrix will now be $2N \times 2N$ instead of $N \times N$, where N is the number of velocity estimates ($N = N_x \times N_y \times N_\zeta$). However, for tests carried out in this study, there were no additional benefits in terms of a more stable solution and it only increased computational time. Therefore the two-step approach is favored. In matrix notation, the above problem is written as

$$\mathbf{A}(\mathbf{u}^\ell) \cdot \mathbf{u}^{\ell+1} = \mathbf{b}(\mathbf{u}^\ell), \tag{48}$$

$$\mathbf{C}(\mathbf{v}^\ell) \cdot \mathbf{v}^{\ell+1} = \mathbf{d}(\mathbf{v}^\ell), \tag{49}$$

where ℓ is the iteration number, **A** and **C** are the coefficient matrices (**A** is formed by the left-hand side of equation (44)), and **b** and **d** are the solution vectors (**b** is formed by the right-hand side of equation (44)).

[17] Starting from a zeroth-order estimate of the horizontal velocity field $\mathbf{u}^0$, a new estimation $\mathbf{u}^1$ of the velocity is obtained by solving the set of linear equations. A quick analysis of the coefficient matrix **A** shows that this matrix is highly sparse: for a horizontal grid of 61×61 nodes and 41 layers in the vertical ($N = 61 \times 61 \times 41 = 152561$), the matrix **A** contains $N \times N$ or more than 23 billion elements, of which at most 2 898 659 elements are strictly nonzero, clustered around the diagonal, which is 0.012% of **A**. Although **A** resembles a band-diagonal matrix, it is more convenient to regard it as a sparse matrix and to solve the linear system of equation (48) using the sparse matrix algorithms of *Press et al.* [1992], which are based on the conjugate gradient method. Although the coding of sparse matrices is rather complicated, they are far more efficient in terms of computation time compared to point relaxation algorithms on the full or even parts of the matrix. A "good" convergence is obtained when the quantity $|\mathbf{A}.\mathbf{u} - \mathbf{b}|/|\mathbf{b}|$ is less than 10^{-4}.

5.1.2. Iterating the Nonlinear System

[18] Because of the nonlinear nature of equation (44) and its transverse counterpart, **A** and **C** contain a parameter that is still a function of u and v, i.e., the viscosity term η, which has to be determined in an iterative fashion. The successive substitution method or Picard iteration might be used for this purpose, but is not favored as values for η vary a few orders of magnitude over the whole ice sheet domain. This puts high demands on the convergence scheme, and may eventually lead to a divergence of the solution. In order to optimize the rate of convergence a relaxation formula was used based on the unstable manifold correction [*Hindmarsh and Payne*, 1996; *Pattyn*, 2002a]. Therefore equation (48) is written as (a similar operation is carried out for equation (49)):

$$\mathbf{A}(\mathbf{u}^\ell) \cdot \mathbf{u}^* = \mathbf{b}(\mathbf{u}^\ell), \tag{50}$$

where $\mathbf{u}^*$ is the velocity estimate obtained with the conjugate gradient method. Consider an iterative solution of a nonlinear equation which generates a series of approximate solutions $\mathbf{u}^{\ell+1}, \mathbf{u}^\ell, \ldots$, being updated by a series of correction vectors $\mathbf{c}^{\ell+1}, \mathbf{c}^\ell, \ldots$, such that $\mathbf{u}^{\ell+1} = \mathbf{u}^\ell + \mathbf{c}^\ell$. Since the correction vector is defined as $\mathbf{c}^\ell = \mathbf{u}^* - \mathbf{u}^\ell$, the Picard iteration would simply update the velocity $\mathbf{u}^{\ell+1}$ with this correction vector, so that $\mathbf{u}^{\ell+1} = \mathbf{u}^*$. If $\mathbf{e}^{\ell+1}, \mathbf{e}^\ell, \ldots$ is taken as the error in the solution vector $\mathbf{u}^{\ell+1}, \mathbf{u}^\ell, \ldots$, then we can state that $(\mathbf{e}^{\ell+1}, \mathbf{e}^\ell, \ldots) = \alpha (\mathbf{c}^{\ell+1}, \mathbf{c}^\ell, \ldots)$. Assuming that the decay is on a straight line in the correction space, we obtain [*Hindmarsh and Payne*, 1996]

$$\alpha = \frac{\| \mathbf{c}^{\ell-1} \|}{\| \mathbf{c}^\ell - \mathbf{c}^{\ell-1} \|}, \tag{51}$$

and a new update of the velocity vector is obtained by

$$\mathbf{u}^{\ell+1} = \alpha \mathbf{u}^* + (1 - \alpha)\mathbf{u}^\ell, \tag{52}$$

where the modified correction vector becomes $\mathbf{c}^\ell_* \approx \alpha\, \mathbf{c}^\ell$. The direction ω between successive correction vectors is computed as

$$\omega = \arccos\left(\frac{\mathbf{c}^\ell \cdot \mathbf{c}^{\ell-1}}{\| \mathbf{c}^\ell \| \cdot \| \mathbf{c}^{\ell-1} \|}\right), \tag{53}$$

where the norms refer to the L_2 norm. Whenever this angle is close to 0 or π, the subspace iteration is applied. Using this subspace relaxation algorithm the solution vector converges properly.

5.2. Ice Sheet Evolution and Thermodynamics

[19] The continuity equation (22) is reformulated as a diffusion equation for ice thickness H. Defining the diffusivities as

$$D_x = \bar{u}H\left(\frac{\partial s}{\partial x}\right)^{-1}, \quad D_y = \bar{v}H\left(\frac{\partial s}{\partial y}\right)^{-1}, \tag{54}$$

the local change in ice thickness is written as

$$\frac{\partial H}{\partial t} - \nabla(\mathbf{D}\nabla H) = \nabla(\mathbf{D}\nabla b) + M_s - M_b, \qquad (55)$$

where $\mathbf{D} = (D_x, D_y)$ is the diffusion vector. Diffusivities are calculated on a staggered grid, where $D_{i+\frac{1}{2}}$ is calculated as the mean of two diffusivities defined on the neighboring grid points i and $i + 1$, and corresponds to the type II diffusivity defined by *Huybrechts et al.* [1996]. Such a scheme is not mass conserving near the edge of the model domain, but is generally more stable than the proper calculation method between grid points (type I). Equation (55) results in a sparse system of $N_x \times N_y$ equations, and is solved using the conjugate gradient method given by *Press et al.* [1992].

[20] The thermodynamic equation (47) is solved implicitly in the vertical, giving rise to a tridiagonal system of N_ζ equations and which is solved using the tridiagonal algorithm of *Press et al.* [1992]. A two-point upstream difference notation was employed for the horizontal, while central differences were used in the vertical. The horizontal implicit terms are found by iteration of this scheme. Only a few iterations are necessary to obtain a good convergence.

6. Experiments and Results

[21] Basic experiments were carried out following the EISMINT benchmark for large-scale ice sheet models, more specifically the ''moving margin'' benchmark of *Huybrechts et al.* [1996]. The model domain is 1500 × 1500 km in the horizontal. Following the EISMINT II experiments [*Payne et al.*, 2000], a grid resolution of 25 km in both horizontal directions was taken, which corresponds to a numerical grid of 61 × 61 grid points. The accumulation/ablation rate M_s is a function of the distance from the ice divide, i.e.,

$$M_s(x,y) = \min\left\{M_{\max}, S_b\left(R_{\mathrm{el}} - \sqrt{(x-x_{\mathrm{sum}})^2+(y-y_{\mathrm{sum}})^2}\right)\right\}, \qquad (56)$$

relax where $M_{\max}$ is the maximum accumulation rate and S_b the gradient of accumulation rate change with horizontal distance. The accumulation rate is zero at a radial distance R_{el} from the summit (x_{sum}, y_{sum}), where x and y are distance in km. At a distance larger than R_{el} from the summit, surface mass balance becomes negative (ablation). The ice surface temperature is also made a function of distance from the summit, according to the benchmark experiments by *Payne et al.* [2000],

$$\theta_s(x,y) = \theta_{\min} + S_\theta\sqrt{(x-x_{\mathrm{sum}})^2+(y-y_{\mathrm{sum}})^2}, \qquad (57)$$

where $\theta_{\min}$ is the minimum surface air temperature and S_θ is the gradient of air-temperature change with distance form the summit. A time step of 20 years was taken for all experiments for the evolution of the continuity equation (55) as well as for the thermodynamic part equation (47). The model was run from zero ice thickness until a steady state was reached (after 200,000 years of calculation). Two types of experiments were carried out with both the HO model (subscript 1) and the SIA model (subscript 0), similar to the experiments described by *Saito et al.* [2003]. Experiment A is the isothermal experiment. Its numerical parameters are listed in Table 2. Experiment B is similar to experiment A, but with thermomechanical coupling, i.e. $A(\theta^*)$ is determined from equation (12). Experiment C is a diagnostic experiment of ice flow over bedrock undulations. Experiment D demonstrates the development of an ice stream within an ice sheet, by considering a frictionless zone ($\tau_b = 0$) at the base of an ice sheet. Another example of a stress-free (lubricated) spot at the base of an ice sheet is the ice flow over a subglacial lake, simulated in experiment E.

Table 2. List of Parameters Used for Experiment A

Parameter	Value	Units
u_b, v_b	0	m yr^{-1}
$A(\theta^*)$	10^{-16}	Pa^{-1} yr^{-1}
$M_{\max}$	0.5	m yr^{-1}
S_b	10^{-2}	m yr^{-1} km^{-1}
R_{el}	450	km
$\theta_{\min}$	238.15	K
S_θ	1.67×10^{-2}	K km^{-1}
x_{sum}, y_{sum}	750	km

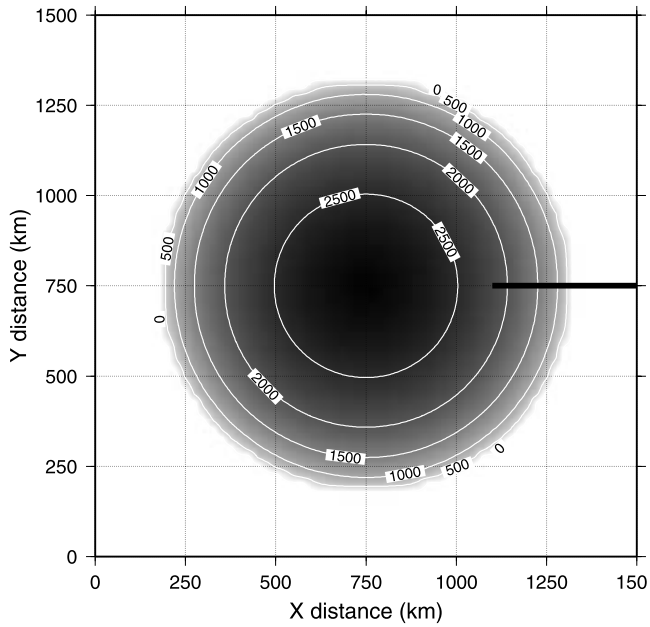

Figure 1. Predicted surface topography of the steady state ice sheet after 200,000 years of integration according to experiment A_1. The thick black line shows the position of the ''ice stream'' for experiment D_1.

6.1. Isotherm Ice Sheet (Experiment A)

[22] Figure 1 displays the surface topography of the ice sheet in steady state for A_1. This ice sheet configuration is similar to the SIA solution A_0, as is expected, since the SIA is valid for large ice sheets resting on a flat bed. The difference between A_1 and A_0 amounts to 10 m (Figure 2). A_1 results in a somewhat smaller ice sheet and has a flatter ice divide. The differences at the divide are traced back to

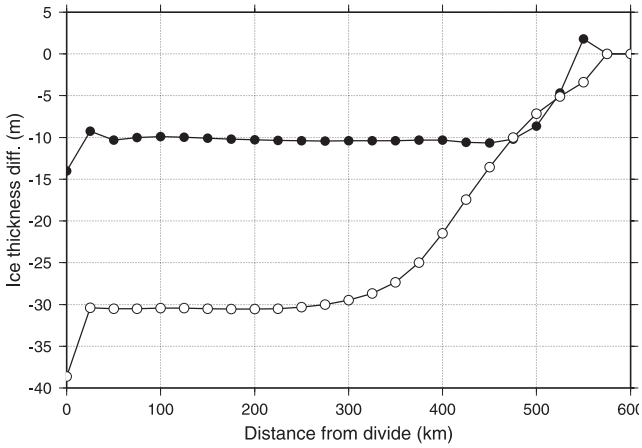

Figure 2. Difference in ice thickness between A_1 and A_0 (solid circles) and between B_1 and B_0 (open circles) after 200,000 years of integration in time.

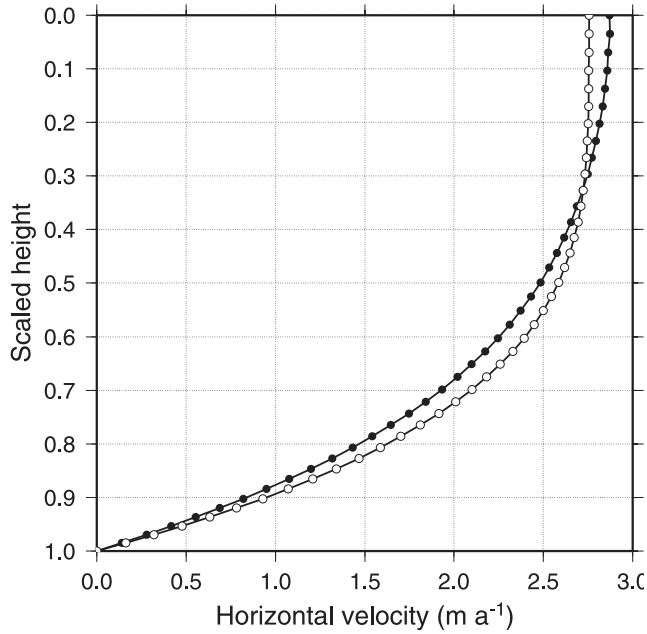

Figure 4. Predicted horizontal velocity at a distance of 25 km from the ice divide for A_1 (solid circles) and A_0 (open circles).

the effect of the inclusion of longitudinal stress gradients in the HO model, which is the only nonzero stress component at the symmetrical ice divide.

[23] The vertical velocity field demonstrates the major difference between both models (Figure 3). A lower vertical velocity under the ice divide for A_1 results in a ''bump'' in the vertical velocity field, confined to the immediate region of the ice divide (Figure 3a). This corresponds to the so-called ''Raymond bump'' [*Raymond*, 1983; *Schøtt Hvidberg*, 1996], due to the fact that ice deep under an ice divide should be very hard and slow to flow, so that upper layers would tend to drape themselves over it. This anomaly in vertical velocity is a result of differences in the horizontal velocity field: close to the ice divide (at 25 km form the divide, Figure 4) surface horizontal velocity is higher for A_1 compared to A_0. However, horizontal velocity at depth is lower than for A_0. This lower velocity is necessary to compensate for the higher surface velocity: as the surface mass balance is only a function of distance from the summit, the steady state ice flux at any point should be the same for both A_0 and A_1. Since ice thickness is similar in both experiments (a difference of only ±10 m), the vertical integrated horizontal velocity should be the same for both models. Further away from the ice divide, the difference in horizontal velocity between both models disappears. The divide anomaly is also observed in the basal temperature: a ''hot spot'' arises underneath the ice divide according to A_1 (Figure 5), due to the difference in vertical advection.

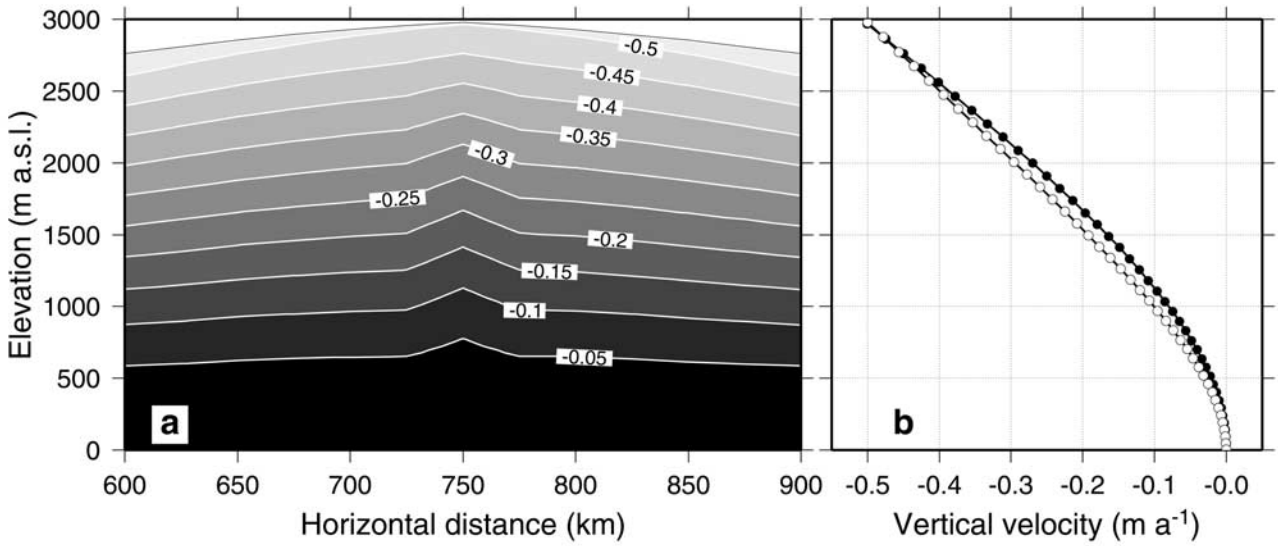

Figure 3. Predicted vertical velocity: (a) near the ice divide for A_1; (b) at the ice divide for A_1 (solid circles) and A_0 (open circles). Note the ''bump'' in vertical velocity at the ice divide, which is not found in A_0.

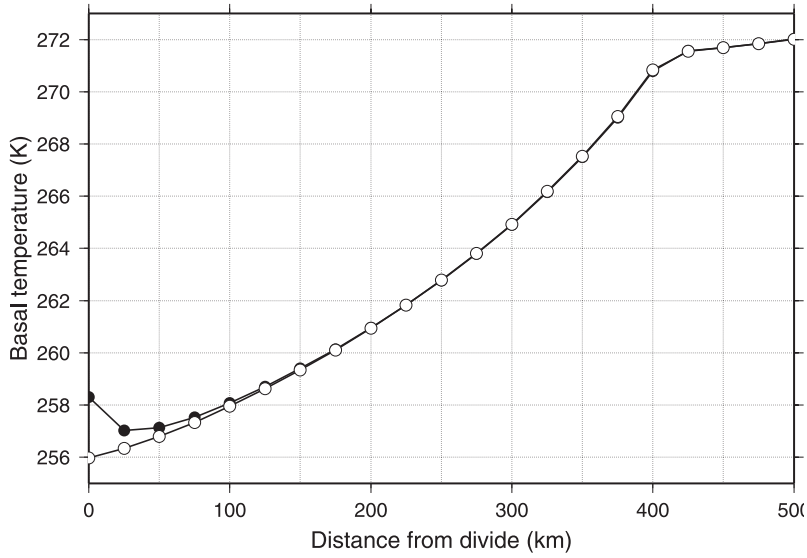

Figure 5. Predicted basal temperature θ_b for A_1 (solid circles) and A_0 (open circles). Note the "hot spot" under the ice divide.

[24] All these results, anomalies in vertical and horizontal flow field and temperature near the ice divide, are corroborated by the experiments carried out by *Saito et al.* [2003]. However, their model results show a slightly thicker A_1 ice sheet, while the present study shows a thinner steady state ice sheet compared to A_0. This difference is probably related to the type of numerical scheme used for the ice sheet evolution equation (55). The hot spot under the divide was determined previously by *Dahl-Jensen* [1989].

6.2. Thermomechanical Coupling (Experiment B)

[25] Results of the thermomechanical coupling (B) are similar to the results of A, i.e., an anomaly in vertical velocity at the divide and a hot spot in the basal temperature profile also occur in B_1. The divide anomaly between both models is more amplified and further generalized within the central part of the ice sheet, as the temperature (and the hot spot) influences the velocity field in a direct way. The difference in ice thickness between B_1 and B_0 is almost 40 m at the divide, and gradually decreases from approximately 300 km from the divide (Figure 2). The smaller ice sheet for B_1 is a direct result of the hot spot at the divide, which leads to softer ice, a higher deformational velocity compared to B_0 and thus a smaller ice sheet. The difference between both models is therefore most pronounced in the interior part of the ice sheet.

[26] The stress field near the ice divide is shown in Figure 6. Shear stress is slightly higher than driving stress,

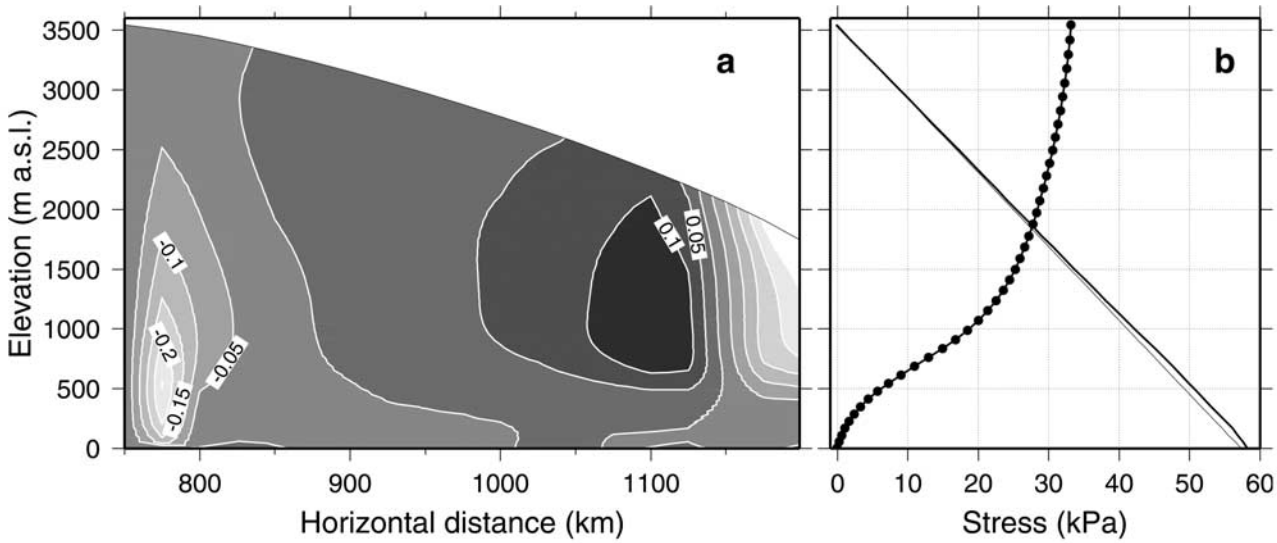

Figure 6. (a) Predicted longitudinal stress gradient $\partial\sigma'_{xx}/\partial x$ (Pa m^{-1}); (b) shear stress σ_{xz} (ζ) (thick solid line), driving stress $\zeta\tau_d$ (thin solid line) and longitudinal stress deviator σ'_{xx} (ζ) (circles) at a distance of 25 km from the ice divide according to B_1.

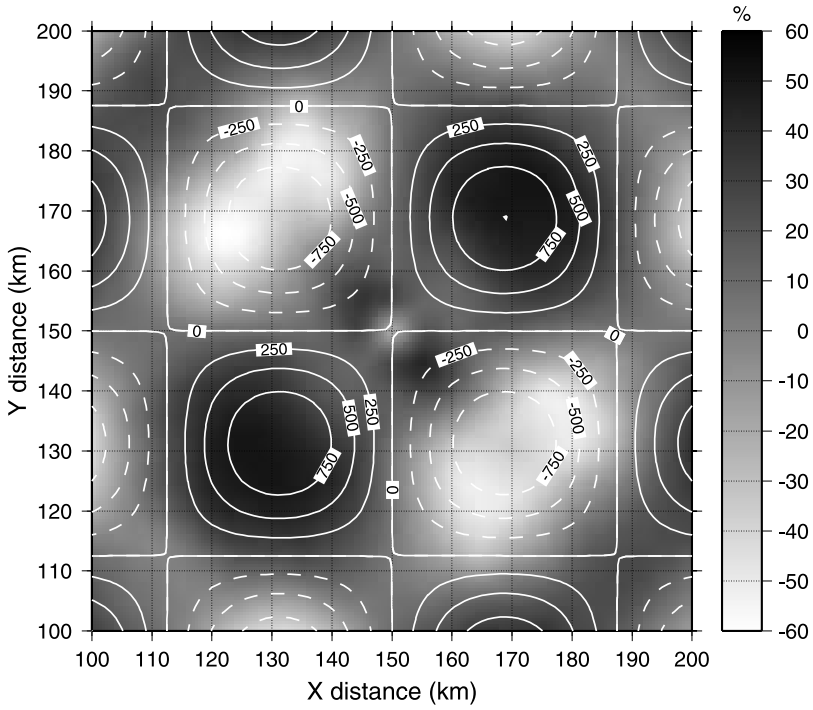

Figure 7. Horizontal surface velocity anomaly $\Delta \mathbf{u}_s = (\mathbf{u}_s(C_1) - \mathbf{u}_s(C_0))/\mathbf{u}s\,(C_1) \times 100$ in the vicinity of the ice divide (x, y = 150,150). Contour lines show basal topography (m).

which means that the longitudinal stress gradient must be negative, although the longitudinal stress is positive as stretching prevails near the ice divide (Figure 6b). The negative stress gradient is a result of the relatively flat ice divide in B_1 and is only present at depth at a horizontal distance of 25 to 100 km away from the ice divide. Further away from the ice divide ($\geq$100 km), the longitudinal stress gradient becomes positive (Figure 6). The overall results of B_1 are in agreement with the results by *Saito et al.* [2003], albeit that some minor differences remain, probably attributed to differences in numerical schemes.

6.3. Ice Flow Over an Undulating Bedrock (Experiment C)

[27] In this diagnostic experiment a similar grid of 61 × 61 grid points was considered, but the horizontal grid size was

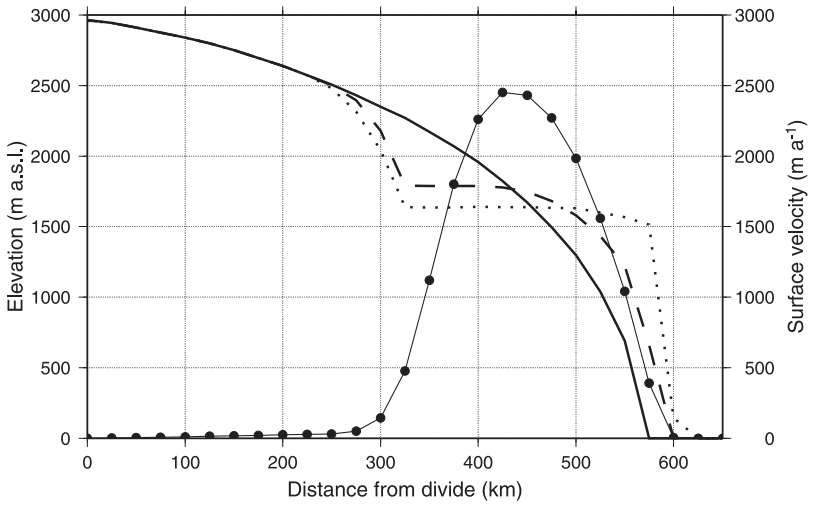

Figure 8. Evolution of an ice stream (D_1) starting from the steady state configuration of A_1. Predicted surface topography at t = 0 (solid line), at t = 50 year (dashed line) and at t = 100 year (dotted line) is displayed, after invoking a stress-free basal condition τ_b = 0 along y = 750 km and between x = 350 km from the divide and the edge of the model domain. Predicted surface velocity at t = 50 year is given in solid circles.

increased to 5 km, thus covering a surface of 300 × 300 km. The surface of the small ice cap is taken from the steady state outcome of experiment A_1. The bedrock is determined from a sine wave function with a double amplitude of 1000 m and a wavelength of 37.5 km. The ice was made stiffer by setting $A(\theta^*)$ equal to 10^{-18} Pa^{-1} yr^{-1}. In this way a high-resolution experiment is carried out in a region of slow ice flow over a highly undulated bedrock. The model geometry was kept constant.

[28] Since the velocity field for C_0 (SIA) is locally determined, it will be solely a function of the local ice thickness and surface gradient (see equation (23)). This implies that the velocity will be high for large ice thickness and/or high surface slopes. The C_1 horizontal velocity field is a smoothed version of C_0, i.e., high velocities in C_0 attain lower values in C_1, and low velocities in C_0 become higher in C_1. These anomalies are associated with the bedrock topography (Figure 7). The maximum (minimum) velocity in C_1 still coincides with the maximum (minimum) velocity in C_0, but longitudinal pushes and pulls, due to the bedrock perturbation, influence the velocity field in a global way and not locally as is the case with C_0. Such smoothing of velocity and stress fields is typical for higher-order models. Similar results were obtained with other higher-order models [*Blatter et al.*, 1998; *Pattyn*, 2002b].

6.4. Ice Stream Evolution (Experiment D)

[29] Starting from the steady state ice sheet conditions and temperature field from experiment A_1, an ice stream was generated by adjusting the basal boundary condition to a stress-free surface (equations (29) and (30)) for the following coordinates: $i = 31$ and $j \geq 45$. The ice stream thus starts at a distance of 350 km from the ice divide and stretches to the edge of the model domain (Figure 1). The width of the ice stream is one grid point, or 25 km.

[30] Figure 8 shows the evolution of the ice stream for the first 100 year after invoking the stress-free boundary conditions. Rather rapidly the ice velocity increases with almost 2 orders of magnitude, to reach maximum values of 2 500 km yr^{-1}, a typical value for an Antarctic ice stream. Also, the surface topography changes dramatically to become almost flat over the whole length of the ice stream. Similar characteristics of ice stream behavior are shown in early flow line models of *Van der Veen* [1987]. The major difference here is that both longitudinal stresses and transverse shear stresses are properly accounted and solved for in three dimensions.

[31] The model result shows a concave inflection point at the onset of the ice stream, similar to the transition between an ice sheet and an ice shelf (Figure 8). It should be noted here that the basal boundary condition applied to our ice stream is similar to that of an ice shelf. Associated with the sudden increase in mass flux is a forward migration of the edge of the ice sheet, forming a frontal "bulge" (Figures 8 and 9a). Basal shear stress is zero along the whole length of the ice stream (Figure 9b). As a result, the surface velocity equals the basal velocity for the whole length of the ice stream (not shown). The longitudinal stress deviator reaches a maximum (extension flow) at the onset of the ice stream and a minimum (compressive flow) at the edge of the ice sheet (Figure 9c), but remains fairly low ($\sigma'_{xx} \sim 0$) along the whole length of the ice stream.

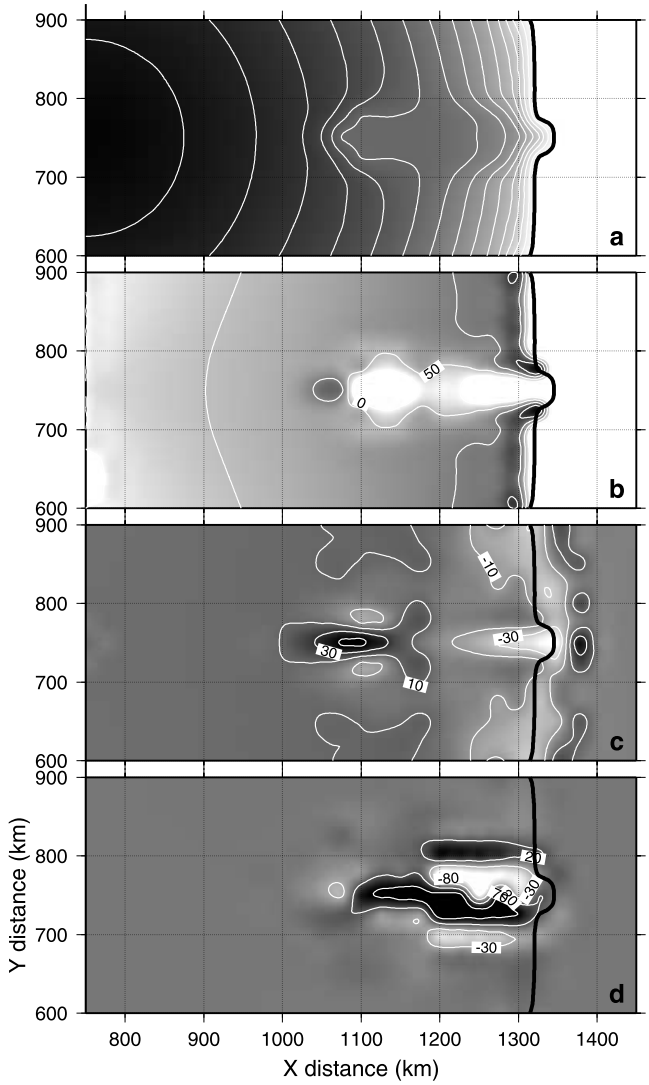

Figure 9. Experiment D_1. (a) Predicted surface topography (m), (b) predicted basal shear stress σ_{xz} (*b*) (kPa), (c) predicted surface longitudinal stress deviator σ'_{xx} (*s*) (kPa), (d) predicted surface transverse shear stress σ_{xy} (*s*) (kPa) at $t = 50$ year. The ice stream is situated at $y = 750$ km and stretches between $x = 1100$ km and the edge of the model domain $x = 1500$ km.

[32] Transverse shear stress shows a pattern that is related to the existence of shear margins and is characterized by high positive values at the southern shear margin of the ice stream and high negative values at the northern shear margin. This results in an important lateral drag over the central part of the ice stream (not shown), which will, due to the absence of the basal shear as well as longitudinal stress gradients, balance the driving stress in the central part of the ice stream. The shear margins are a consequence of the rapid ice flow embedded in the slow moving ice sheet. Both patterns of longitudinal and transverse shear stress are typical features for existing Antarctic ice streams, such as the Siple Coast ice streams [*Whillans and Van der Veen*, 1997] albeit that the magnitude of the marginal shear stress (20–80 kPa in Figure 9) is relatively small compared to the

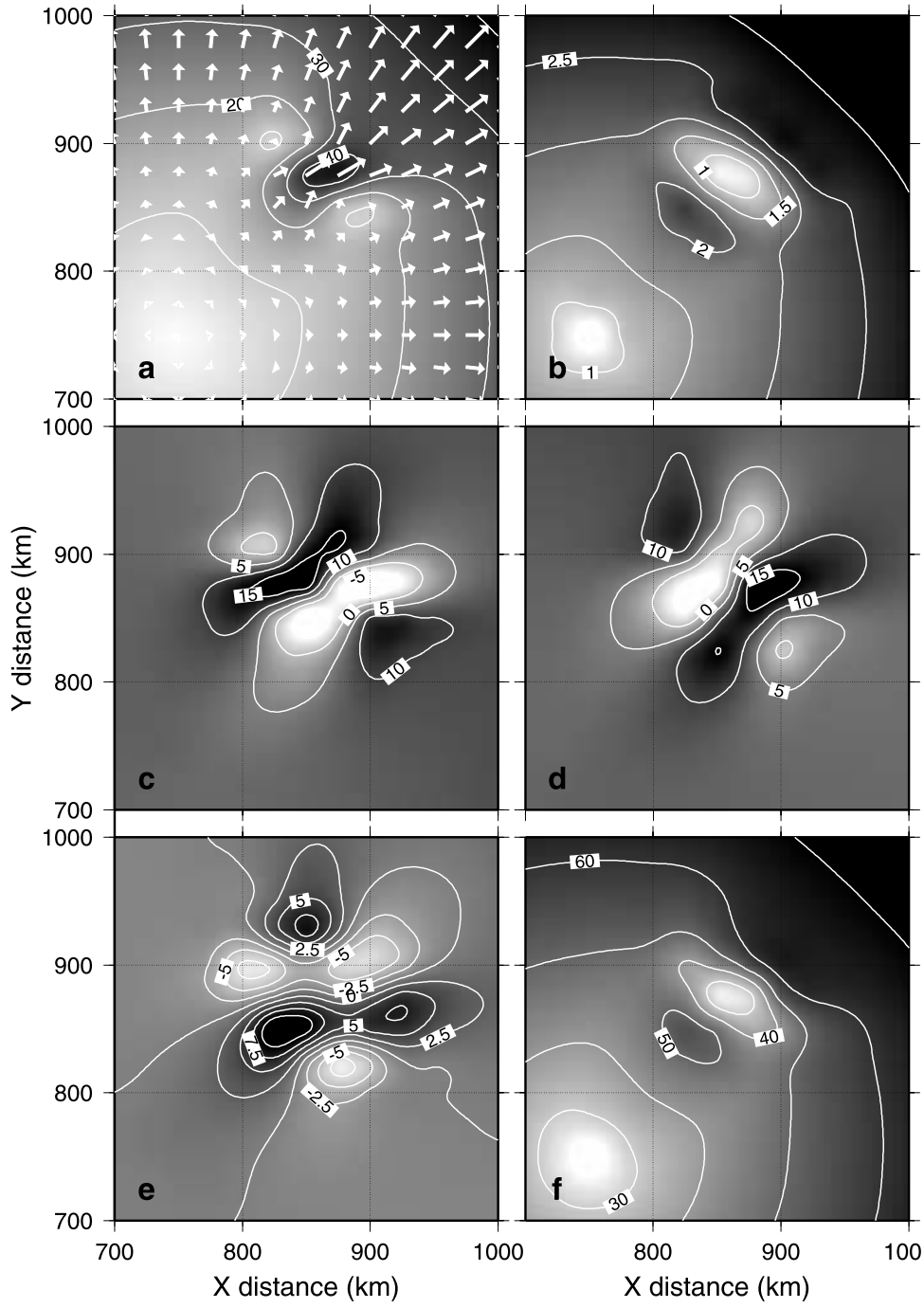

Figure 10. Experiment E_1. (a) Predicted surface velocity (m yr^{-1}), (b) predicted surface slope ($\times 10^3$), (c) predicted surface longitudinal stress deviator σ'_{xx} (s) (kPa), (d) predicted surface longitudinal stress deviator σ'_{yy} (s) (kPa), (e) predicted surface transverse shear stress σ_{xy} (s) (kPa), (f) predicted basal shear stress $(\sigma_{xz}^2\ (b) + \sigma_{yz}^2\ (b))^{1/2}$. The ice divide is situated at (x, y) = (750, 750) km. The lake is situated at (x, y) = (875, 875) km and is 50 km long in x and 25 km wide in y.

magnitude of marginal shear stresses calculated for modern Antarctic ice streams.

6.5. Ice Flow Over a Subglacial Lake (Experiment E)

[33] Radio echo sounding in East Antarctica has revealed the existence of numerous subglacial lakes. The largest one is Lake Vostok (14,000 km^2), near the homonymous Russian Station and drilling site. Lake Vostok is associated with a prominent morphological surface feature within the Antarctic ice sheet, as the ice sheet surface is relatively flat and featureless, consistent with the surface of an ice shelf. Ice flow over a large subglacial lake should be analogous to the flow of an ice shelf, where the lack of basal shear stress prevents deformation of internal layers [*Siegert et al.*, 2000]. Other distinct features of the ice flow over Lake Vostok are revealed by the surface velocity field determined

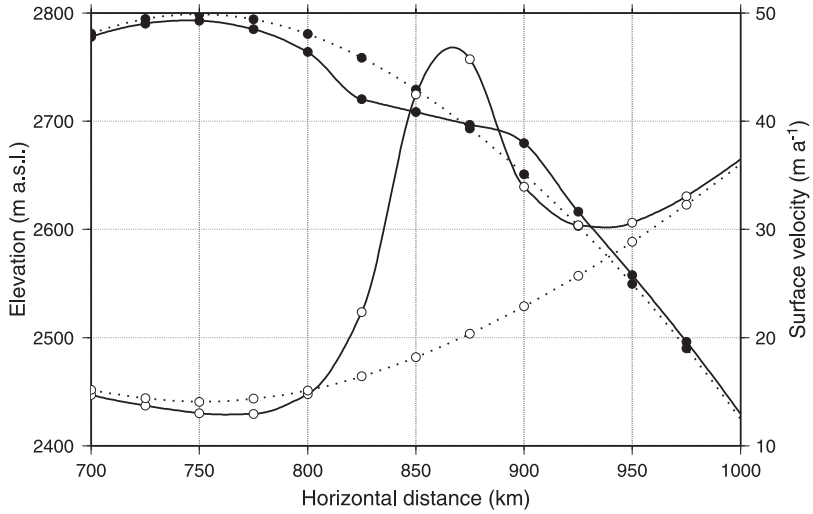

Figure 11. Evolution of a subglacial lake in the central region of the ice sheet (E_1) starting from the steady state configuration of A_1. Predicted surface topography (solid circles) without lake (dashed line) and over a lake (solid line). Surface velocities (open circles) without (dashed line) and over a lake (solid line). The lake is situated at (x, y) = (875, 875) km and is 50 km long in x and 25 km wide in y.

from radar interferometry [*Kwok et al.*, 2000]: (1) an increase in ice velocity over the lake (extension flow) followed by a decrease in ice speed passed the lake (compression flow), and (2) a slight turning of the ice flow over the lake, most visible over the central part of Lake Vostok where surface slopes are small. Model simulations of the ice flow at Lake Vostok demands the use of a HO model. *Mayer and Siegert* [2000] investigated the ice flow along a longitudinal transect with a 2-D HO flow line model. Their results demonstrate that ice dynamics across the inflow grounding line are similar to an ice sheet/ice shelf transition.

[34] Experiment E_1 thus consists of simulating the ice flow over a subglacial lake with the 3-D HO model by considering a stress-free basal surface (lubricated spot) stretching over two grid points and situated approximately 100 km from the ice divide. The orientation of the so-called subglacial lake with respect to the major ice flow is similar to the situation of Lake Vostok. The initial conditions are given by experiment A_1 and the ice sheet was allowed to react to the change in basal boundary conditions until the ice sheet surface reached a steady state. Results of E_1 indicate that the surface velocity over the subglacial lake increases to reach a maximum near the center of the lake, and decreases again at the downstream edge of the lake (Figure 10a). Moreover, the ice sheet flow field seems only locally influenced by the presence of the lake, as the velocities downstream from the lake are similar to those if no lake were present (Figure 11). These findings are corroborated by *Siegert and Ridley* [1998] and by the measurements of *Kwok et al.* [2000]. Also the turning of the ice flow is visible in experiment E_1, as the surface slope of the lake depends on the orientation of the lake toward the surrounding ice flow. The maximum slope is therefore found in the longitudinal direction of the lake.

[35] A flattening of the surface topography above the lake is observed in Figures 10b and 11, conform observations in Antarctica [*Siegert et al.*, 2000], which is associated with a low basal shear stress (Figure 10f). The zone of influence of other stress components (longitudinal and transverse stresses, Figures 10c, 10d, and 10e) is much larger than the effective area occupied by the lake. These stress components show a distinct "butterfly" pattern that extents for more than 100 km in either horizontal direction.

7. Discussion and Conclusions

[36] The numerical model developed and presented here is a three dimensional thermomechanical ice sheet model including higher-order (HO) stress gradients. Similar HO models exist, most of them solving for the stress field, using the method proposed by *Van der Veen and Whillans* [1989] and *Van der Veen* [1989]. The uniqueness of this model lies in the fact that it solves the force balance equations in their 'derivative' form, by formulating them in terms of velocity gradients (using Glen's flow law) and solving second derivatives analytically instead of numerically. The resulting equations look rather cumbersome, but assure a high numerical stability. Stability of the numerical scheme can be further improved by adapting upstream differences for velocity gradients in the effective viscosity.

[37] Basic experiments with the model include the standard EISMINT I benchmark experiments [*Huybrechts et al.*, 1996] as well the EISMINT II experiments with thermomechanical coupling [*Payne et al.*, 2000]. A comparison is made with a similar 3-D model according to the SIA, and both isothermal and thermomechanical experiments are considered. Results are in agreement with results from *Saito et al.* [2003], and the solution under the ice divide (Raymond bump and hot spot) is confirmed by earlier flow line studies [*Raymond*, 1983; *Dahl-Jensen*, 1989]. Model experiments by *Schøtt Hvidberg* [1996] were carried out at much higher detail and show the rise of isochrons (due to reduced vertical velocity with a HO model) 1 to 2 ice thicknesses from the ice divide. The model resolution of the present study (25 km) does not

allow to identify the span of the Raymond bump, as the grid point closest to the divide is at least 8 ice thicknesses away. However, the solution right under the ice divide remains correct, irrespective of horizontal model resolution. Similar remarks can be made for the rising basal temperatures under the divide, associated with the reduced vertical advection.

[38] With the exception of the ice-flow-over-a-bumpy-bed experiment, all model runs are prognostic, which keeps an internal consistency between the conservation equations. Two examples of prognostic model runs that can only be solved with a HO model are the ice stream development and the ice flow over a subglacial lake, both simulated by considering locally a stress-free basal surface. Changing from a basal stress dominated regime to a basal stress-free regime is similar to the ice sheet/ice shelf/grounding line problem, which remains a hot topic amidst the ice sheet modeling community. For instance, *Marshall and Clarke* [1997] solved this problem by treating the ice sheet area as a binary mixture of sheet ice (shallow ice approximation) and stream ice (vertically integrated force balance equations), which reduces the model complexity. In the present model a proper treatment of the transition zone is given, as the ice mass is considered as one single continuum. In reality, the reduction of basal drag in an ice stream is a complex process involving basal hydrology, sediment deformation, basal melting and sliding, which lies beyond the scope of this paper. The simple basal boundary switch seems sufficient to explain major processes that are observed in real ice masses. For simulations of existing glaciers and ice sheets, more complex basal boundary conditions will become necessary.

[39] A major deficiency of the model runs remains the low grid resolution used (with the exception of the ice-flow-over-a-bumpy-bed experiment). For instance, the model lake occupies only two grid points, which is insufficient to draw solid conclusions. Nevertheless, the simulation is successful, since major characteristics of the ice flow over a subglacial lake, such as Lake Vostok, are represented. The situation at Lake Vostok is also slightly different from the model lake over a flat bedrock, as Lake Vostok lies in a subglacial trench and the bedrock slope near the grounding line dips toward the lake. Since major components of the flow field could be simulated, this indicates that the stress-free basal boundary condition is a decisive factor in the ice dynamics over a subglacial lake, and not the geometric configuration. The fact that the 'real' lake lies in a subglacial trench overlain by thick ice adds to the insulation effect and might be responsible for high basal temperatures, hence ensuring the presence of a subglacial lake.

[40] **Acknowledgments.** This paper forms a contribution to the Belgian Research Programme on the Antarctic (Federal Office for Scientific, Technical and Cultural Affairs), contract EV/03/08A, and a contribution to the "European Project for Ice Coring in Antarctica (EPICA)", a joint European Science Foundation/European Commission (EC) scientific programme, funded by the EC under the Environment and Climate Programme and by national contributions from Belgium, Denmark, France, Germany, Italy, Netherlands, Norway, Sweden, Switzerland, and the United Kingdom.

References

Albrecht, O., Dynamics of glaciers and ice sheets: A numerical model study, Ph.D. thesis, Swiss Fed. Inst. of Technol., Zurich, 2000.

Baral, D., K. Hutter, and R. Greve, Asymptotic theories of large-scale motion, temperature, and moisture distribution in land-based polythermal ice sheets: a critical review and new developments, *Appl. Mech. Rev.*, *54*, 215–256, 2001.

Blatter, H., Velocity and stress fields in grounded glaciers: A simple algorithm for including deviatoric stress gradients, *J. Glaciol.*, *41*, 333–344, 1995.

Blatter, H., G. Clarke, and J. Colinge, Stress and velocity fields in glaciers: Part II. sliding and basal stress distribution, *J. Glaciol.*, *44*, 457–466, 1998.

Budd, W., The longitudinal stress and strain-rate gradients in ice masses, *J. Glaciol.*, *9*, 19–27, 1970a.

Budd, W., Ice flow over bedrock perturbations, *J. Glaciol.*, *9*, 29–48, 1970b.

Budd, W., Stress variations with ice flow over undulations, *J. Glaciol.*, *10*, 177–195, 1971.

Colinge, J., and H. Blatter, Stress and velocity fields in glaciers: part I. finite-difference schemes for higher-order glacier models, *J. Glaciol.*, *44*, 448–456, 1998.

Dahl-Jensen, D., Steady thermomechanical flow along two-dimensional flow lines in large grounded ice sheets, *J. Geophys. Res.*, *94*, 10,355–10,362, 1989.

Dansgaard, W., and S. Johnsen, A flow model and a time scale for the ice core for Camp Century, Greenland, *J. Glaciol.*, *8*, 215–223, 1969.

Greve, R., Application of a polythermal three-dimensional ice sheet model to the Greenland ice sheet: Response to steady-state and transient climate scenarios, *J. Clim.*, *10*, 901–918, 1997.

Hindmarsh, R., Influence of channelling on heating in ice-sheet flows, *Geophys. Res. Lett.*, *28*, 3681–3684, 2001.

Hindmarsh, R., and A. Payne, Time-step limits for stable solutions of the ice-sheet equation, *Ann. Glaciol.*, *23*, 74–85, 1996.

Hooke, R., Flow law for polycrystalline ice in glaciers: Comparison of theoretical predictions, laboratory data, and field measurements, *Rev. Geophys.*, *19*, 664–672, 1981.

Hutter, K., *Theoretical Glaciology*, Kluwer Acad., Norwell, Mass., 1983.

Huybrechts, P., A 3-D model for the Antarctic ice sheet: A sensitivity study on the glacial-interglacial contrast, *Clim. Dyn.*, *5*, 79–92, 1990.

Huybrechts, P., and T. Payne, The EISMINT benchmarks for testing ice-sheet models, *Ann. Glaciol.*, *23*, 1–12, 1996.

Kwok, R., M. Siegert, and F. Carsey, Ice motion over Lake Vostok, Antarctica: Constraints on inferences regarding the accreted ice, *J. Glaciol.*, *46*, 689–694, 2000.

Lliboutry, L. A., *Very Slow Flows of Solids*, Martinus Nijhoff, Zoetermeer, Netherlands, 1987.

Marshall, S., and G. Clarke, A continuum mixture model of ice stream thermomechanics in the Laurentide ice sheet: 1. Theory, *J. Geophys. Res.*, *102*, 20,599–20,614, 1997.

Mayer, C., Numerische Modellierung der Übergangszone zwischen Eisschild und Shelfeis (numerical modelling of the transition zone between an ice sheet and an ice shelf), *Ber. Polarforsch.*, *214*, 1–150, 1996.

Mayer, C., and M. Siegert, Numerical modelling of ice-sheet dynamics across the Vostok subglacial lake, central East Antarctica, *J. Glaciol.*, *46*, 197–205, 2000.

Paterson, W., *The Physics of Glaciers*, 3rd ed., Oxford, Pergamon, Tarrytown, N.J., 1994.

Pattyn, F., Ice-sheet modelling at different spatial resolutions: Focus on the grounding line, *Ann. Glaciol.*, *31*, 211–216, 2000.

Pattyn, F., Transient glacier response with a higher-order numerical ice-flow model, *J. Glaciol.*, *48*, 467–477, 2002a.

Pattyn, F., Ice-flow characteristics over a rough bedrock: Implications for ice-core interpretation, *Polar Meteorol. Glaciol.*, *16*, 42–52, 2002b.

Payne, A., et al., Results from the EISMINT model intercomparsion: The effects of thermomechanical coupling, *J. Glaciol.*, *46*, 227–238, 2000.

Press, W., S. Teukolsky, W. Vetterling, and B. Flannery, *Numerical Recipes in C: The Art of Scientific Computing*, 2nd ed., Cambridge Univ. Press, New York, 1992.

Raymond, C., Deformation in the vicinity of ice divides, *J. Glaciol.*, *29*, 357–373, 1983.

Ritz, C., A. Fabre, and A. Letréguilly, Sensitivity of a Greenland ice sheet model to ice flow and ablation parameters: Consequences for the evolution through the last glacial cycle, *Clim. Dyn.*, *13*, 11–24, 1997.

Saito, F., Development of a three dimensional ice sheet model for numerical studies of Antarctic and Greenland ice sheet, Ph.D. thesis, Univ. of Tokyo, Tokyo, 2002.

Saito, F., A. Abe-Ouchi, and H. Blatter, Effects of the first order stress gradients to an ice sheet evaluated by a three-dimensional thermomechanical coupled model, *Ann. Glaciol.*, *37*, in press, 2003.

Schøtt Hvidberg, C., Steady-state thermomechanical modelling of ice flow near the centre of large ice sheets with the finite- element method, *Ann. Glaciol.*, *23*, 116–123, 1996.

Siegert, M., and J. Ridley, An analysis of the ice-sheet surface and subsurface topography above the Vostok Station subglacial lake, central East Antarctica, *J. Geophys. Res.*, *103*, 10,195–10,207, 1998.

Siegert, M., R. Kwok, C. Mayer, and B. Hubbard, Water exchange between the subglacial Lake Vostok and the overlying ice sheet, *Nature*, *403*, 643–646, 2000.

Van der Veen, C., Longitudinal stresses and basal sliding: A comparative study, in *Dynamics of the West Antarctic Ice Sheet*, edited by C. Van der Veen and J. Oerlemans, pp. 223–248, Kluwer Acad., Norwell, Mass., 1987.

Van der Veen, C., A numerical scheme for calculating stresses and strain rates in glaciers, *Math. Geol.*, *21*, 363–377, 1989.

Van der Veen, C., and I. Whillans, Force budget: I. theory and numerical methods, *J. Glaciol.*, *35*, 53–60, 1989.

Whillans, I., and C. Van der Veen, The role of lateral drag in the dynamics of Ice Stream B, Antarctica, *J. Glaciol.*, *43*, 231–237, 1997.

F. Pattyn, Department of Geography, Vrije Universiteit Brussel, Pleinlaan 2, B-1050 Brussel, Belgium. (fpattyn@vub.ac.be)